Solar-Terrestrial Physics. 2025, vol. 11, iss. 4, pp. 104–115. DOI: 10.12737/stp-114202511. © 2025
D.A. Pavlov, M.B. Krainev, M.S. Kalinin, A.V. Kodukov, Xi Luo, Fang Shen, Yuji Zhu. Published by INFRA-M Academic Publishing House

DOI: 10.12737/stp-114202511

Received June 08, 2025
Accepted August 06, 2025

MHD-SIMULATION OF COROTATING INTERACTION REGIONS IN THE HELIOSPHERE USING DIFFERENT BOUNDARY CONDITIONS AND CODES

D.A. Pavlov
St. Petersburg State Electrotechnical University "LETI", St. Petersburg, Russia, dapavlov@etu.ru
St. Petersburg State University, St. Petersburg, Russia

M.B. Krainev
Lebedev Physical Institute RAS, Moscow, Russia, mkrainev46@mail.ru

M.S. Kalinin
Lebedev Physical Institute RAS, Moscow, Russia, kalininms@lebedev.ru

A.V. Kodukov
St. Petersburg State Electrotechnical University "LETI", St. Petersburg, Russia, akodukovich@mail.ru

Xi Luo
Shandong Institute of Advanced Technology, Jinan, Shandong, China, xi.luo@iat.cn

Fang Shen
State Key Laboratory of Space Weather, National Space Science Center CAS, Beijing, China, fshen@spaceweather.ac.cn

Yuji Zhu
Shandong Institute of Advanced Technology, Jinan, Shandong, China, yjzhu@spaceweather.ac.cn

Abstract. The paper presents the results of MHD modeling of corotating interaction regions (CIRs) at distances of 0.1 AU from the Sun (inner boundary) to much larger distances (20–30 AU) in two variants in which the magnetic field on the photosphere (1) is determined from a detailed synoptic map and (2) is represented only by the dipole component. The calculations are made for Carrington rotation 2066 (January–February 2008), using two independent software packages of Russian and Chinese groups. The time period under study is characterized by the presence of long-lived coronal holes on the Sun and a stable recurrent variation in heliosphere characteristics, as well as in the intensity of galactic cosmic rays.

We discuss the advantages and disadvantages of modeling CIRs by detailed and dipole models of the photospheric magnetic field, as well as with the two mentioned software packages. The mechanisms of formation and evolution of CIRs with distance in the two models are compared and correlated to the conclusions of our previous works.

Keywords: heliosphere, corotating interaction regions (CIRs), MHD simulation of CIRs, detailed and dipole CIR models.

INTRODUCTION

Corotating interaction regions (CIRs) are large-scale structures in the solar wind (SW), which occur when faster streams from coronal holes interact with slower streams associated with equatorial streamer structures. This interaction leads to plasma accumulation, appearance of standing shock waves, strong density, velocity, and interplanetary magnetic field strength gradients. CIRs typically comprise a forward compression front, a high turbulence region, possible backward fronts, and generally cross the heliospheric current sheet (HCS). Due to solar rotation, such structures are recurrent and are observed with a period ~27 days. Their significance goes beyond local near-Earth manifestations: CIRs have a major effect on propagation and modulation of both galactic (GCR) and solar (SCR) cosmic rays, as well as on the formation of the heliospheric structure at distances up to several tens of astronomical units [Gosling, Pizzo, 1999; Potgieter, 2013]. This makes CIR modeling an important area of research in heliophysics, especially in problems related to space weather forecasting and particle modulation.

CIRs have been studied for more than fifty years [Belcher, Davis, 1971; Richardson, 2018]. A significant amount of observations have been accumulated, mainly in Earth's orbit, but also (occasionally) to large heliographic latitudes [Forsyth, Gosling, 2001] and distances [Hundhausen, Gosling, 1976; Burlaga et al., 1984]. Shortly after the discovery of CIRs and the relationship of high-speed SW streams with coronal holes and low-speed streams with streamer structures in the corona, onto crests of which the heliospheric current sheet is projected, MHD models of CIRs were developed including the formation of a contact surface, standing shock waves, a spatial change in structure, etc. [Pizzo, Gosling, 1994; Gosling, Pizzo, 1999]. Many works have been devoted to these calculations, but they are mainly aimed at predicting near-Earth characteristics of the heliosphere and are limited to small distances from the Sun (within r=1÷2 AU) [http://www.swpc.noaa.gov/products/wsa-enlil-solar-wind-prediction; http://solarwind.entroforce.ru; Arutyunyan et al., 2023].

Nonetheless, besides being important for setting near-Earth space weather parameters, CIRs represent a

separate phenomenon and seem to have a significant effect on characteristics of the heliosphere in its main volume (outside Earth's orbit) [Krainev et al., 2023]. Due to the fact that spacecraft are very rare in this volume, of particular importance in studying CIRs may be the interpretation of their associated GCR intensity variations, which, even when recorded near Earth, pass both inside CIR and through the middle and far heliosphere on their way to it.

Since in order to simulate GCR intensity variations related to CIRs a model of the heliosphere with due regard to CIRs, in particular to large distances, should first be constructed, such two-stage modeling (of heliospheric characteristics in the MHD approximation, and then the GCR intensity from the results) has been carried out in a number of works [Wiengarten et al., 2014; Kopp et al., 2017; Guo, Florinski, 2014, 2016; Luo et al., 2020, 2023, 2024]. At the same time, approaches to solving this problem and the results obtained differ significantly in some aspects.

In this paper, as well as in [Krainev et al., 2023; Kalinin et al., 2023, 2024], we analyze the results and develop the approaches adopted in [Luo et al., 2020, 2023, 2024]. We discuss two approaches to MHD modeling of CIRs and the results of this modeling performed by two research teams. Section 1 formulates and analyzes the system of MHD equations, the procedure for setting boundary conditions at the inner boundary, selects the period for simulating CIR, explores advantages and disadvantages of choosing two photospheric magnetic field models, and discusses the results of CIR simulation by these models with the Russian team's software package. Section 2 presents the results of a similar CIR simulation for the same period, carried out by the Chinese team. When presenting the CIR simulation results, we consider only two vector heliospheric characteristics: SW velocity and heliospheric magnetic field (HMF), which are important for cosmic ray propagation. Finally, Section 3 discusses the results of the previous sections and draws conclusions.

1. MHD MODELING OF CIRs BY THE RUSSIAN TEAM

1.1. Selection of photospheric magnetic field period and models

First, let us draw some conclusions in terms of the phenomena under discussion. Strictly speaking, the terms “corotating interaction regions” and “recurrent variations of characteristics” connote that CIRs rotate with the Sun, and time profiles of heliospheric characteristics and GCR intensity (when observed from Earth) repeat each other for successive solar rotations. This means that in the coordinate system rotating with the Sun distributions of heliospheric characteristics and GCR intensity are stationary. There is no strict repetition for successive rotations in observations of the characteristics of both the heliosphere and GCRs. We can, however, utilize their longitude distributions, averaged over several solar rotations, as a first approximation to this requirement. Thus, for MHD modeling to $r=r_{MHD}$ it is desirable to use boundary conditions at the inner boundary of the heliosphere ($r_{in}\approx 0.1$ AU), averaged approximately over $K=r_{MHD}/\Delta r$ solar rotations, where $\Delta r = 6$ AU is the layer through which SW of average speed passes during one solar rotation, and to compare the calculation results with the observation results averaged over this period.

The calculations were made for CR2066 (January 25 – February 21, 2008). The time period under study is marked by presence of long-lived coronal holes on the Sun and a stable recurrent variation in heliospheric characteristics, as well as in GCR intensity [Modzelewska et al., 2020].

The Wilcox Solar Observatory (WSO) catalog has been chosen as a source of maps of the photospheric magnetic field, which provides solutions of the equations of potential field source surface (PFSS) 2.5 R_s [Schatten et al., 1969]), in particular for average conditions of Carrington rotations [http://wso.stanford.edu/Harmonic.los/ghlist.html]. Hereafter, R_s stands for the photosphere radius. The solutions are presented in the form of coefficients of the associated Legendre polynomials [http://wso.stanford.edu/words/pfss.pdf] up to degree and order 9 inclusive, which makes it easy to choose the details of the photospheric magnetic field model in use from maximum degree. In this work, we have employed two models: with harmonics up to degree 8 ($l_{max}=8$) and up to degree 1 ($l_{max}=1$). The former model for detailing magnetic fields on the photosphere is closer to real conditions for a particular solar rotation, but we think that many of these details are relatively short-lived and should be smoothed when averaged over several rotations. The latter model represents the magnetic field in the shape of tilted dipole, i.e. in the complete absence of these details. Note that the model of titled dipole is widely used to determine the shape of the heliospheric current sheet when modeling GCR intensity variations [Potgieter, 2013], as well as to examine the effect of CIRs on the time profile of GCR intensity [Zhu et al., 2024]. In this paper, the model of tilted dipole was employed primarily to verify the results of calculations performed with a more detailed model of photospheric magnetic field, as well as to identify and analyze patterns of CIR formation and evolution in space and time. Due to its simplicity and regularity, the model of tilted dipole can identify the main features of the behavior of heliospheric parameters and thus serves as a kind of reference when interpreting the results obtained in more complex models.

1.2. Equations and technical parameters of MHD simulation

In this paper, interplanetary plasma is modeled using “ideal” MHD equations, i.e. those that do not contain diffusion and resistivity:

$$\frac{\partial \rho}{\partial t} + \nabla \cdot \mathbf{m} = 0, \tag{1}$$

$$\frac{\partial \mathbf{m}}{\partial t} + \nabla \cdot \left[\mathbf{m}\mathbf{v}^T - \mathbf{B}\mathbf{B}^T + I\left(p + \frac{B^2}{2} \right) \right]^T = \tag{2}$$

$$= \rho \mathbf{g} - 2\boldsymbol{\Omega} \times \mathbf{m} - \rho \boldsymbol{\Omega} \times \left(\boldsymbol{\Omega} \times \mathbf{r} \right),$$

$$\frac{\partial \mathbf{B}}{\partial t} - \nabla \times \left(\mathbf{v} \times \mathbf{B} \right) = 0, \tag{3}$$

$$\frac{\partial E_t}{\partial t} + \nabla \cdot \left[\left(\frac{\rho v^2}{2} + p \frac{\gamma}{\gamma - 1} \right) \mathbf{v} - \left(\mathbf{v} \times \mathbf{B} \right) \times \mathbf{B} \right] = \\ = \mathbf{m} \cdot \left(\mathbf{g} - \mathbf{\Omega} \times \left(\mathbf{\Omega} \times \mathbf{r} \right) \right), \tag{4}$$

$$E_t = \frac{\rho}{\gamma - 1} + \frac{m^2}{2\rho} + \frac{B^2}{2}, \tag{5}$$

where ρ is the proton density, **v** is the velocity, **m**=ρ**v** is the momentum per unit volume, p is the pressure, **B** is the magnetic field, **g** is the free fall acceleration, **Ω** is the angular velocity of coordinate system. The temperature T is not directly included in the equations, but it is related to density and pressure by the equation of state $p = k\rho T / \left(m_u \mu \right)$, where k is the Boltzmann constant, m_u is the atomic mass unit, μ=0.616 is the average molar mass of particles, γ=1.5 is the adiabatic exponent. The magnetic constant μ_0 is absent in (2) because μ_0=1 in the chosen system of units.

A general approach to MHD modeling is presented in [Arutyunyan et al., 2023]. The PLUTO package [Mignone et al., 2007] and the numerical scheme implemented in it based on the solution of the Riemann problem by the Harten—Lax—van Leer (HLL) method are used for modeling.

The simulation mesh has the following dimensions and partitioning:

- By radial coordinate: from 0.1 to 20 AU, 2100 cells (l_{max}=1) or to 7 AU, 1200 cells (l_{max}=8);
- By latitude: from 0 to 180°, 180 cells;
- By longitude: from 0 to 360°, 360 cells.

Partitioning by longitude and latitude is uniform, whereas by the radial coordinate it is logarithmic, described by the law

$$r_{i+1} = r_i \left(\frac{r_{MHD}}{r_{in}} \right)^{1/N}, \tag{6}$$

where r_i is the mesh node (i=0...N), while r_{in}=21.5R_s and r_{MHD}=r_N are the inner (0.1 AU) and outer CIR boundaries respectively.

PLUTO has built-in support for longitude and latitude boundary conditions: periodic and polaraxis respectively. An outflow boundary condition is set at the outer boundary in the radial coordinate. Conditions at the inner boundary are described in Subsection 1.5.

A stationary (rotating with the Sun) coordinate system is also available in PLUTO. The coordinate system rotation period is set to be 24.47 days (solar rotation period at the equator). Thus, the solar surface in this coordinate system is stationary, and the boundary conditions at the inner boundary of the simulation area are constant. The corresponding terms of Coriolis acceleration and centripetal acceleration are added to the MHD equations.

1.3. B_r map on the photosphere

The solution of the potential field equations for the radial component provided by WSO is as follows [http://wso.stanford.edu/words/pfss.pdf]:

$$B_r\left(r, \theta, \phi\right) = \\ = \sum_{lm} \overline{P_l^m}\left(\cos\theta\right)\left(g'_{lm}\cos\left(m\phi\right) + h'_{lm}\sin\left(m\phi\right)\right) \times \\ \times \left[\left(l+1\right)\left(\frac{R_s}{r}\right)^{l+2} + l\left(\frac{r}{R_{ss}}\right)^{l-1}\left(\frac{R_s}{R_{ss}}\right)^{l+2} \right],$$

where g'_{lm} and h'_{lm} are the coefficients provided by WSO (in particular, at [http://wso.stanford.edu/Harmonic.los/CR2066] coefficients for CR2066 are given); l, m are degree and order of the associated Legendre polynomial respectively; R_{ss}=2.5R_s is the source surface radius. The coefficient g'_{00} (monopole) is ignored.

Note that the associated Legendre polynomials are normalized in WSO as follows:

$$\int_{-1}^{1} \left(\overline{P_l^m}\left(x\right) \right)^2 dx = \frac{2}{2l+1}\left(2 - \delta_{m0}\right),$$

which is different from the commonly used normalization

$$\int_{-1}^{1} \left(P_l^m\left(x\right) \right)^2 dx = \frac{2\left(l+m\right)!}{\left(2l+1\right)\left(l-m\right)!}.$$

Thus, the associated Legendre polynomials in WSO are calculated from common ones, using the relation

$$\overline{P_l^m}\left(x\right) = \left(-1\right)^m \sqrt{\frac{\left(l-m\right)!}{\left(l+m\right)!}\left(2-\delta_{m0}\right)} P_l^m\left(x\right).$$

Although the WSO solution is available on the source surface (r=R_{ss}) too, we employ the WSO map on the photosphere (r=R_s), and further calculations, including PFSS model calculations, are made by other means.

1.4. Construction of a 3D map of the magnetic field in the solar corona

The PFSS model as an acceptable reduction of the solar magnetic field model to 2.5R_s [Hoeksema, 1984; Riley et al., 2006] has many implementations, both analytical and numerical. In analytical implementations, the solution of the Laplace equation is obtained by calculating the coefficients of spherical harmonics, whereas in numerical implementations the solution is constructed as a map on a discrete mesh. In this paper, due to the need to trace field lines, we have chosen the second approach, realized in the POT3D package [https://github.com/predsci/POT3D] by the finite element method.

At a greater distance from the Sun, the assumption of potentiality does not apply, and the Schatten Current Sheet (SCS) model [Schatten, 1971] is used to simulate the magnetic field between 2.5 R_s and 21.5 R_s (0.1 AU), in which currents are supposed to be between magnetic field regions of opposite polarity. The model employs the following assumption: from 2.5 R_s field lines no longer close on the photosphere. In this regard, B_r is set positive (outgoing) in all regions, even in those where PFSS has specified negative polarity. POT3D is employed to calculate the SCS model.

1.5. Tracing field lines and calculating the V_r map at the inner boundary of the heliosphere

The radial SW velocity component on the 2.5 R_s source surface is given by the empirical WSA (Wang—Sheeley—Arge) model [Wang, Sheeley, 1990; Arge, Pizzo, 2000])

$$V_r\left(2.5, \theta_{2.5}, \phi_{2.5}\right) = 285 + \frac{625}{\left(1+f_s\right)^{2/9}} \times$$

$$\times\left(1-0.8\exp\left(-\left(\theta_b/2\right)^2\right)\right)^3 \text{ km/s},$$

where $f_s = \left(\frac{1}{2.5}\right)^2 \frac{B_r\left(2.5, \theta_{2.5}, \phi_{2.5}\right)}{B_r\left(1, \theta_1, \phi_1\right)}$ is the coefficient of expansion of magnetic tubes of open magnetic field lines between the photosphere and the source surface, and θ_b is the angular distance (in degrees) from the lower point of field line (θ_l, ϕ_l) to the coronal hole boundary. Thus, θ_b, determined on the photosphere, is mapped on the source surface by tracing field lines. Similarly, by tracing field lines from 21.5 R_s to 2.5 R_s, the V_r map constructed on the source surface is transposed into the outer boundary of the simulation field. Tracing is performed three times by the streamtracer package [https://github.com/sunpy/streamtracer]:

1. Down from 21.5 R_s to 2.5 R_s in the 3D magnetic field map calculated by the SCS model. The starting points are the centers of cells of a uniform mesh of longitudes and latitudes ($\theta_{21.5}$, $\phi_{21.5}$).

2. Down from 2.5 R_s to 1 R_s in the 3D magnetic field map calculated by the PFSS model. The starting points are the ends of the lines obtained at the previous stage ($\theta_{2.5}$, $\phi_{2.5}$). The cells of the uniform mesh of latitudes and longitudes on the photosphere, in which ends of the lines appear, are marked as coronal hole regions. All lines that have reached the source surface are assumed to be open (Wang, Sheeley, 1990).

3. Upward from 1R_s to 2.5 R_s (Figure 1) in the 3D magnetic field map calculated by the PFSS model. The starting points are the centers of cells of the uniform mesh of longitudes and latitudes, which were not considered coronal holes according to the results of tracing 2. When the line has reached the source surface, the cell is also marked as a coronal hole region (Figures 2, 3).

1.6. Boundary and initial conditions in the heliosphere

At the inner boundary of the MHD simulation field (r_{in}=0.1 AU), maps of two vector quantities (**B**, **V**) and two scalar quantities (numerical particle density D, pressure p) must be specified. The following values are preset: V_r (see Subsection 1.5), $V_\phi = V_\theta = 0$, $|B_r| = 4.5\cdot10^{-7}$ T. The polarity in each mesh is equal to the polarity at the end of the field line traced from 21.5 R_s to the source surface [Nikolic, 2017] (see Subsection 1.5):

$$B_\phi = -B_r \Omega \sin\theta \, 2\pi 21.5 R_s / V_r, \quad B_\theta = 0,$$

$$D = D_{fast} V_{fast} / V_r, \; p = k D_{fast} T_{fast} / (m_u \mu).$$

The value of V_{fast}=750 km/s used in the SW prediction model of the Solar Weather Prediction Center (SWPC) was taken. B_r, as well as D_{fast}=400 cm^{-3}, T_{fast}=1.5·10^6 K are close in order of magnitude to those

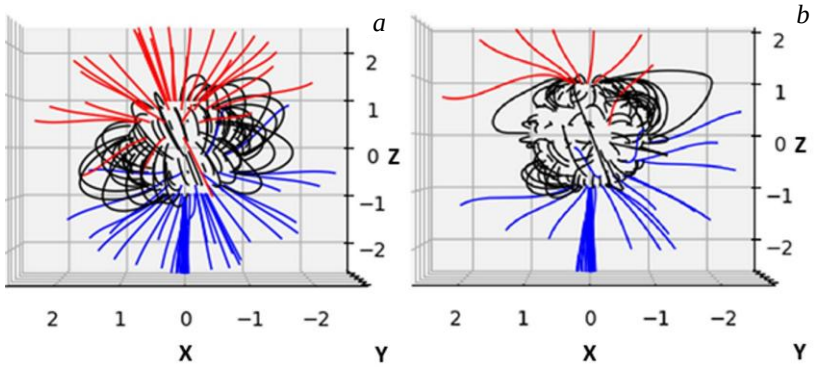

Figure 1. Results of tracing of magnetic field lines from 1 R_s to 2.5 R_s for the WSO model with L_{max}=1 (*a*) and L_{max}=8 (*b*). Red lines are open field lines with B_r<0; blue lines, with B_r>0; black lines indicate closed field lines

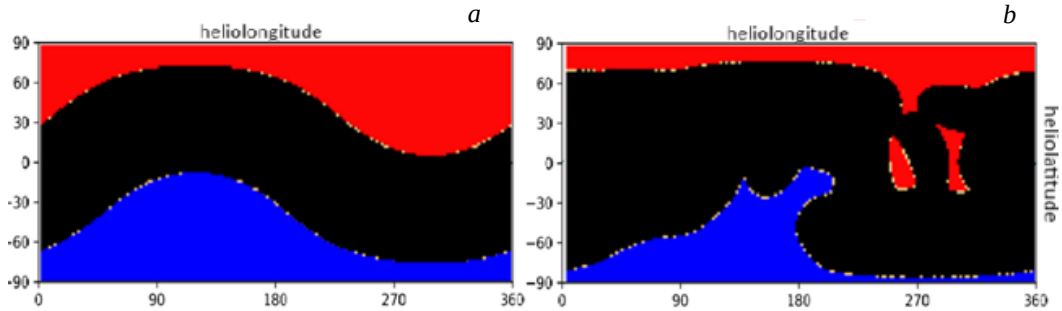

Figure 2. Polarity of magnetic field lines: L_{max}=1 (*a*); L_{max}=8 (*b*). Red fill denotes negative open field lines; blue, positive open field lines; black, closed field lines; yellow, incorrectly defined closed field lines, corrected in upward tracing

measured during CR2066 (given the extrapolation from 1 to 0.1 AU). The initial conditions in the 3D MHD simulation field were prescribed as follows:

$$V_r(r,\theta,\phi) = V_r(r_{in},\theta,\phi), \quad (7)$$

$$V_\phi(r,\theta,\phi) = -\Omega r_{in}\sin(\theta), \quad (8)$$

$$V_\theta(r,\theta,\phi) = 0, \quad (9)$$

$$B_r(r,\theta,\phi) = B_r(r_{in},\theta,\phi_0)\left(\frac{r_{in}}{r}\right)^2, \quad (10)$$

$$B_\phi(r,\theta,\phi) = -B_r(r_{in},\theta,\phi_0)\left(\frac{\Omega 21.5R_s}{V_r}\right)\left(\frac{r_{in}}{r}\right), \quad (11)$$

$$B_\theta(r,\theta,\phi) = 0, \quad (12)$$

$$D(r,\theta,\phi) = D(r_{in},\theta,\phi)\left(\frac{r_{in}}{r}\right)^2, \quad (13)$$

$$p(r,\theta,\phi) = p(r_{in},\theta,\phi_0)\left(\frac{r_{in}}{r}\right)^3, \quad (14)$$

$$\phi_0 = \phi + \frac{r - r_{in}}{V_r(r_{in},\theta,\phi)}\Omega\sin\theta. \quad (15)$$

These initial conditions are similar to the stationary equations of Parker spirals [Parker, 1958] and to the initial conditions used in [Wang et al., 2020; Luo et al., 2020]. Differences between these initial conditions and the indicated sources, as well as differences between the sources, are not important since the final result of MHD simulation (stationary pattern) does not depend on the initial conditions that can only affect the convergence rate.

1.7. MHD modeling results

The formation and evolution of CIRs with distance calculated by two models of photospheric magnetic field from WSO data for CR2066 are illustrated in Figure 3. The more complete model is seen to provide a much larger number of regions of strengthening and weakening of more complex HMF than the simple model. Moreover, in the more detailed model, variations of velocity and HMF are much deeper and develop much faster than in the simple model.

The difference between the maps for the two models is particularly pronounced in a more significant disturbance of the HCS shape with distance for the detailed model. Since we attribute this disturbance to disadvantages of MHD modeling of HCS as an important characteristic of CIRs, CIR calculations in the WSO model with L_{max}=8 at r>7 AU were not carried out. However, even for the simple WSO model with L_{max}=1, small disturbances form in HCS already at 4 AU and persist to r=7 AU. What happens to the B_r and V_r maps in the simple model over long distances can be seen in Figure 4.

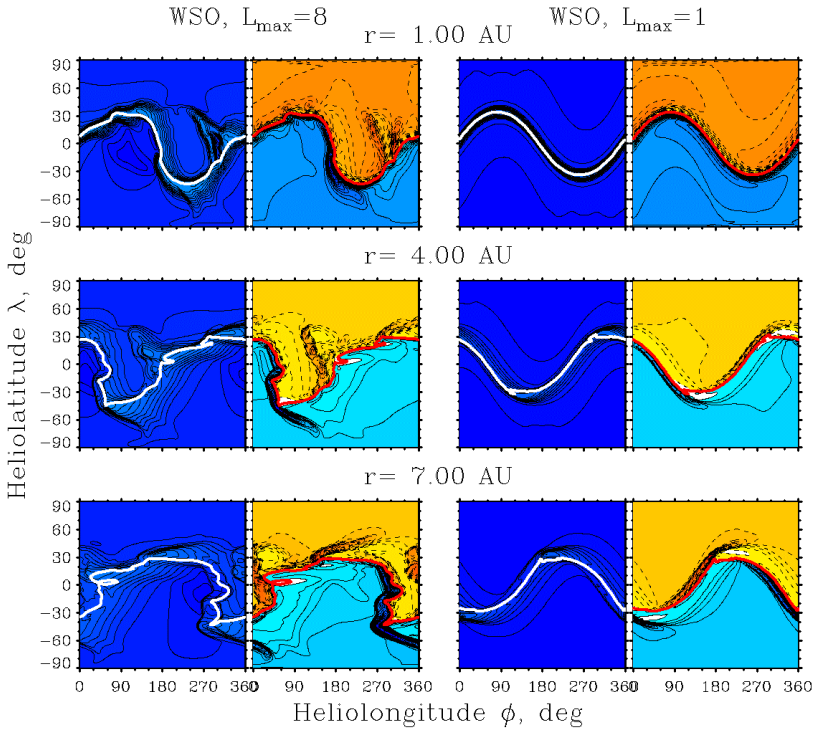

Figure 3. Formation and evolution of CIRs with distance calculated by the Russian team adopting two models of photospheric magnetic field from WSO data for CR2066 with allowance for harmonics up to L_{max}=8 (left) and L_{max}=1 (right) in the inner heliosphere (top), at r=4 AU (middle) and r =7 AU (bottom). Each panel presents maps of radial SW velocity (left) and HMF induction (right). On the magnetic field maps, the hemisphere B_r>0 is marked with shades of blue and with solid isolines; and B_r<0, with shades of yellow and red with dashed isolines. The correspondence of the shade to the value (omitted in the Figure) is the same for the corresponding maps of both models. The red line indicates HCS separating the unipolar hemispheres B_r (isolines B_r=0); on V_r maps, HCS is shown by the white line

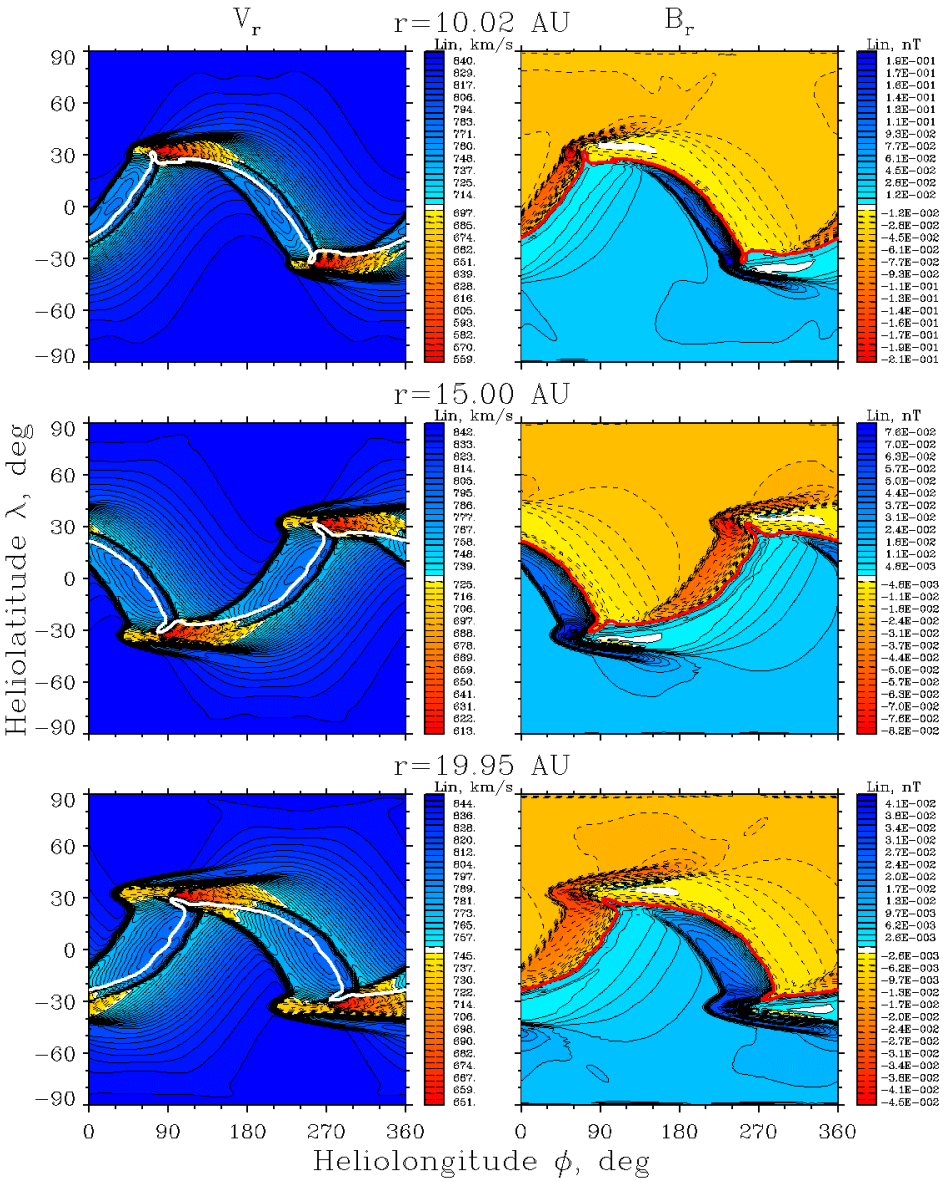

Figure 4. Comparison between distributions of radial SW velocity and HMF induction according to WSO data with L_{max}=1 at larger heliocentric distances than in Figure 3. Location of the maps in the panels, as well as the type of isolines and HCS lines are the same as in Figure 3. The correspondence of the color to the characteristic value is shown to the right of each panel

Figures 3 and 4 illustrate the formation and evolution of radial SW velocity and HMF induction. At distances greater than a few AU, the HMF and SW velocity direction (in the coordinate system rotating with the Sun) becomes more and more azimuthal, but V_φ, as well as the value and polarity of B_φ are primarily determined by the B_r and V_r maps according to (9).

Distributions of the polar components V_ϑ and B_ϑ and their evolution with distance (Figure 5) may, nonetheless, be important characteristics of model CIR. These distributions are seen to be quite complex and there is a component in the distribution of their polarity that follows the B_r polarity distribution quite closely, as judging by the position of the B_r=0 line. Another, higher-latitude V_ϑ component indicates that the SW stream is poleward already from r=10 AU.

2. FORMATION AND EVOLUTION OF CIRs IN CHINESE MODELS

Similar MHD modelings of CIRs for CR2066 and other solar rotations by the detailed model of solar magnetic field (SMF) from GONG data were carried out by the Chinese team [Luo et al., 2020, 2023, 2024], using a technique detailed in [Shen et al., 2018]. Basically, the CIR modeling technique was similar to that adopted by the Russian team (described in Section 1): The results of SMF scanning and the empirical WSA technique were utilized as initial data for setting boundary conditions for SW velocity; boundary conditions for other characteristics were consistent with observations from the Earth orbit; system of MHD equations (1)–(5) was solved over the entire range of polar and azimuthal angles to r_{MHD}

with known numerical methods. Some differences were found with the method described in Section 1:

- The systems of MHD equations partially differ, Equation (4) in [Shen et al., 2018] describes a pressure change; whereas Equation (4) in the MHD model used by PLUTO, a change in energy density;
- Use of a 6-component mesh to detect singularities at the poles, the configuration of the mesh along the radius is poorly known, only 88 points are available for analysis;
- The Chinese team implemented the potential field model, using a system of equations for spherical harmonic coefficients, while the Russian team employs the POT3D package in which the potential field model is realized by the finite element method;
- Different coefficients for the WSA model, some of which are calibrated depending on the solar cycle phase;
- The set of invariants and free parameters in forming boundary conditions differs from those discussed in Section 1;
- Different value of adiabatic exponent (γ=1.46);

To maintain the condition ∇B=0 in the Russian model, an additional source is included in the equations [Powell et al., 1999], whereas the Chinese team applied an artificial diffusion method.

Note that in [Shen et al., 2018] the technique adopted by the Chinese team in their studies was applied to modeling of heliospheric characteristics up to r=1.25 AU, and it provides the best description of observations of heliospheric characteristics in the vicinity of the Earth orbit. In addition, from the results of CIR modeling for CR2066 with the two cited models by the Chinese team, we had only a sample for certain distances, which was used to simulate the GCR intensity.

Figure 6 compares the maps of radial SW velocity and HMF components calculated for CR2066 by GONG models with L_{max}=8 ([Luo et al., 2020]; left panels) and with L_{max}=1 (this work; right panels) at three heliocentric distances.

As already discussed in [Krainev et al., 2023], where CIR and GCR modeling results obtained in [Luo et al., 2020] for CR2066 by the GONG model with Lmax=8 were analyzed, CIR evolution leads to strong and sharp HCS flattening (see the left middle panel in Figure 6),

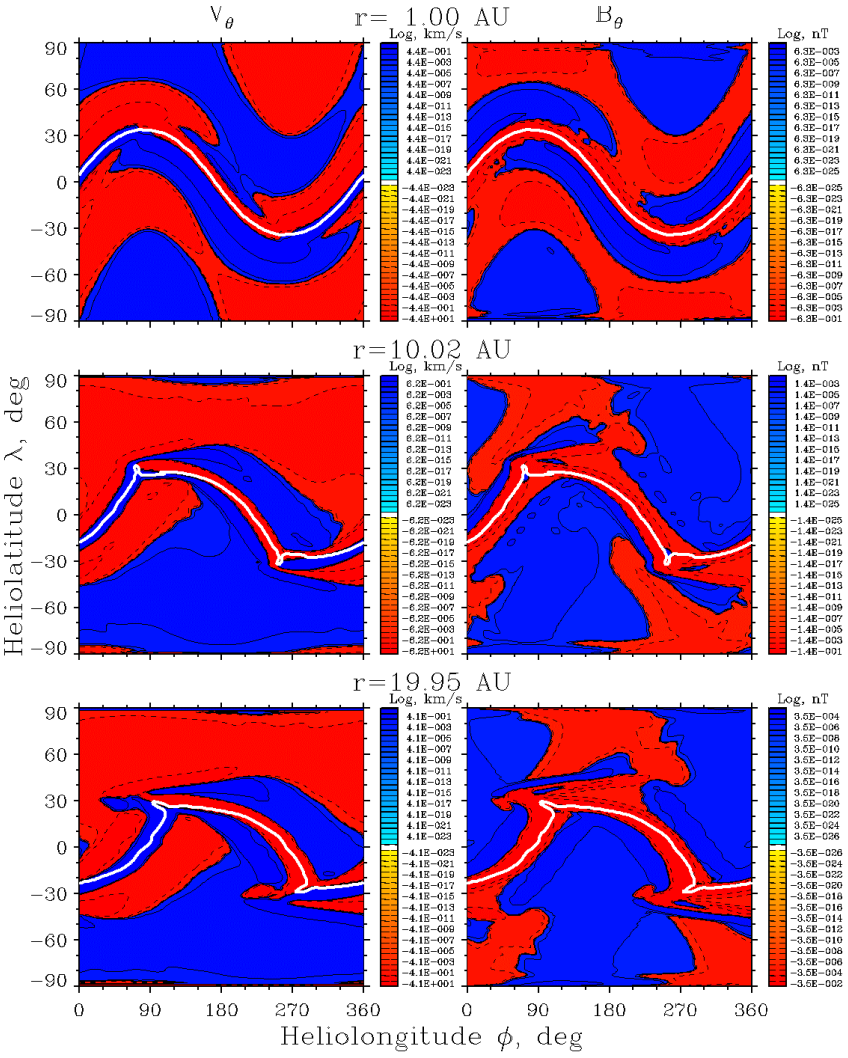

Figure 5. Distribution of polar components of SW velocity (left) and HMF induction (right) according to WSO data with L_{max}=1 at different heliocentric distances. Isoline types are the same as in Figures 3, 4. The correspondence of the shade to the characteristic value is shown to the right of each panel. The isolines B_r=0, indicated by the white line on both V_ϑ and B_ϑ maps, are presented as HCS lines.

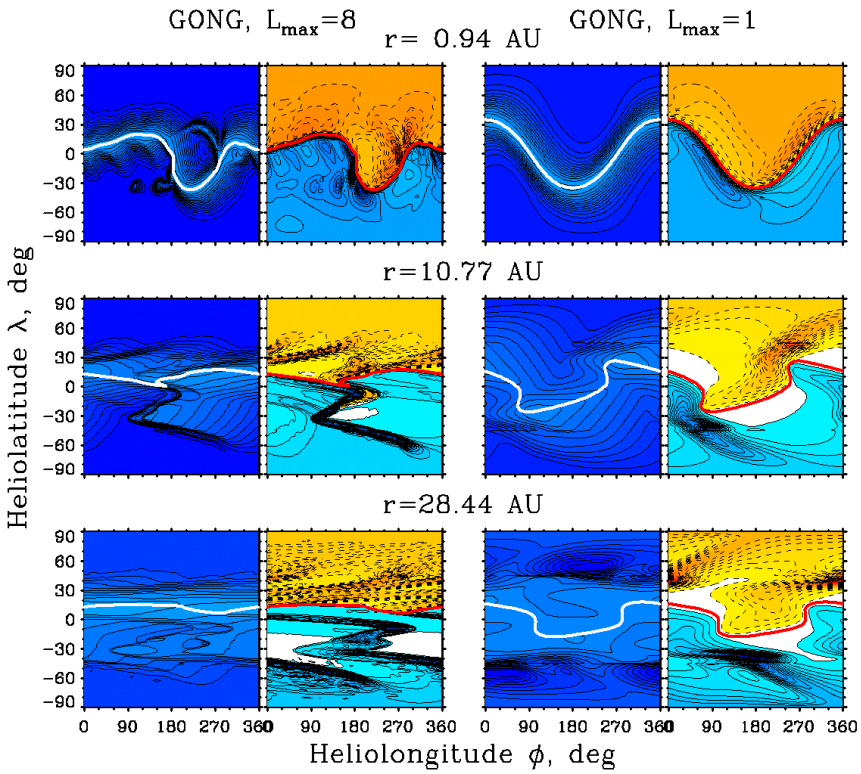

Figure 6. CIR formation and evolution with distance calculated by the Chinese team when employing two photospheric magnetic field models from GONG data for CR2066 with allowance for harmonics up to L_{max}=8 (left panels) and L_{max}=1 (right panels) from the inner heliosphere to the outer MHD- simulation boundary. Location of the maps in the panels, as well as the shades of color, isolines, and HCS lines are the same as in Figure 3

as well as to a significant change of the HMF radial component modulus distribution with distance and a general decrease in HMF strength averaged over longitude. Gradual HCS flattening and a change in B_r distribution are also seen in the right panels of Figure 6. Yet, it is difficult to obtain a general picture of the heliocentric distance dependence of HMF characteristics from the maps for individual distances presented in Figure 6. Figure 7 illustrates this dependence, as well as the relative weakening of HMF due to CIR, for detailed and dipole models. As in [Krainev et al., 2023], Parker HMF corresponding to its radial component at the inner boundary of the heliosphere and to the SW velocity on this surface averaged over longitude was utilized as HMF strength in the absence of CIRs:

$$\Delta_{Par}^{MHD}(r,\theta,\varphi) = \frac{\left(B^{MHD}(r,\theta,\varphi) - \overline{B}^{Par}(r,\theta,\varphi)\right)}{\overline{B}^{Par}(r,\theta,\varphi)} \cdot 100\ \%. \quad (16)$$

Top panels in Figure 7 indicate that from several astronomical units the HCS tilt, i.e. half of the latitude range in which the HCS is located, systematically decreases. At the same time, for the detailed model (L_{max}=8, left panel), after a gradual decrease from 3 to 10 AU, the tilt decreases sharply due to separation and disappearance of the "island" of B_r<0 (see the middle left panel in Figure 6). Then, the tilt continues to gradually decrease. For the dipole model (L_{max}=1, right panel), the HCS tilt gradually decreases from ~35° to 15° without any dramatic jumps.

To find the cause for such a systematic decrease in the sectoral structure zone, we analyzed maps of distribution of the polar components V_ϑ and B_ϑ and their evolution with distance illustrated in Figure 8. It is obvious that these distributions are quite complex and distributions of their polarity differ significantly from the distribution of the B_r polarity, which can be judged by the position of the B_r=0 line. As for the Russian CIR model, high-latitude and low-latitude components can be identified in the behavior of V_ϑ. For the high-latitude component, the poleward SW stream is not as uniform in longitude as in the Russian model, and it reverses at other longitudes. However, for the low-latitude component V_ϑ the SW stream is fairly uniform in longitude and directed toward the equator.

3. DISCUSSION AND CONCLUSIONS

All the CIR models discussed are based on the results of scanning of the solar magnetic fields for CR2066, i.e. for the period when long-lived coronal holes existed on the Sun, and the persistent 27-day variation was observed in heliospheric characteristics and GCR intensity. The CIR models differed, first, in the degree of detail of SMFs forming the basis for the modeling, and, second, in initial SMF data, software packages, and algorithm details used by the Russian and Chinese teams to model CIRs.

As for the degree of detail of SMFs, to calculate the SW velocity at the inner boundary of the heliosphere both teams employed 1) more detailed data taking into

account the terms in the Legendre polynomial expansion of the SMF radial component on the photosphere up to L_{max}=8, and 2) the most simplified data accounting only for dipole terms, i.e. to L_{max}=1. As already mentioned, due to the strong perturbation of the HCS shape for the detailed model at r=4÷7 AU, the Russian team did not calculate CIR in the model with L_{max}=8 at r>7 AU. It is natural that the overall distribution pattern of all heliospheric characteristics for the detailed SMF model is much more complex than for the dipole model. Nonetheless, on closer examination, it is possible to identify both similarities and differences.

1. At the inner boundary of the heliosphere, the distributions of characteristics (especially the SW velocity) according to the full-field model contain much more details, and the HCS shape is more complex. The feature in common is that the position of the global SW velocity minimum coincides with the HCS line. However, for the detailed model, in addition to this global velocity minimum there are many local ones, whereas for the dipole model there are no other SW velocity minima.

2. In both models, at short distances (to r=1÷2 AU), HMF strengthens to the west of HCS, and weakens to the east. The combination of these two phenomena illustrates the mechanism of CIR formation and their genetic relationship with HCS.

3. At middle distances (to r=4÷7 AU), in addition to CIRs containing HCS, their extensions are formed at higher latitudes (hockey-stick-like, i.e. with a kink), without HCS. With increasing distance, this process of separation of CIR from HCS that formed it continues, and at long distances the regions of enhanced HMF concentrate at middle latitudes (approximately coinciding with the latitudinal boundaries of HCS on the inner surface of the heliosphere), and at higher and lower latitudes HMF weakens.

4. At middle and long distances, two components of meridional SW streams are formed: high-latitude and low-latitude, the boundaries between which also roughly coincide with the latitudinal boundaries of HCS on the inner surface of the heliosphere. Uniformity of these streams in longitude is different for CIRs calculated by the Russian and Chinese teams (see below); however, in general, the high-latitude SW stream is poleward, and the low-latitude one is equatorward.

The CIR models calculated by the Chinese team have the following features.

5. From middle distances, the half-width of the latitude range occupied by HCS, i.e. tilt, decreases significantly. For more complex structures formed in the detailed model, the island of opposite polarity may break away (and then disappear) and HCS will become significantly flatter. This does not happen in the dipole model, but by the boundary of the MHD modeling region, the tilt decreases by about half. In addition, analysis of the evolution of different SW velocity and HMF components with distance leads to the conclusion that the HCS shape changes considerably.

6. In both models, the longitude velocity gradient decreases with distance (replaced by the latitude gradient), i.e. the source of CIRs weakens.

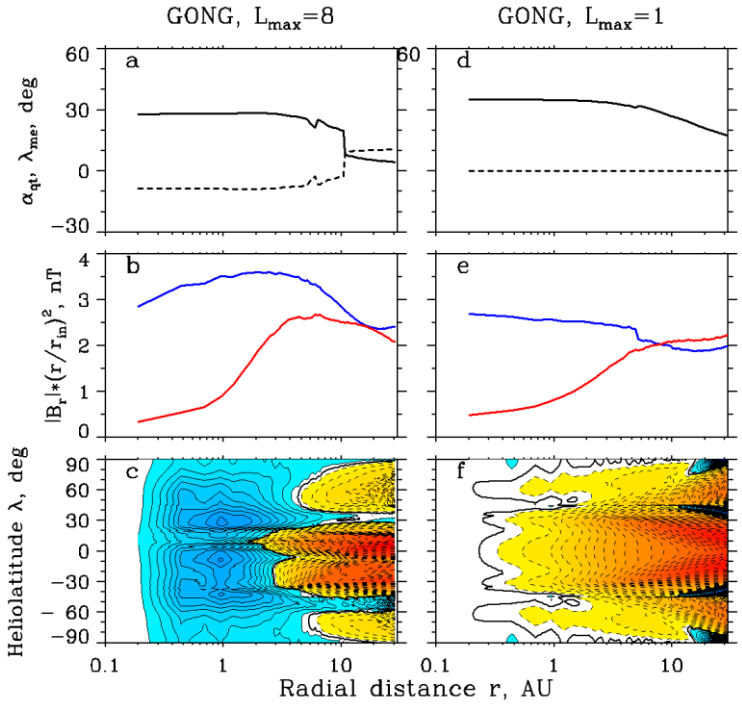

Figure 7. Dependence of HMF characteristics on heliocentric distance for detailed (L_{max}=8, *a*–*c*) and dipole (L_{max}=1, *d*–*f*) models. Panels *a*, *d* show the half-width of the latitude range occupied by HCS (the so-called tilt, solid black line) and the latitude of the middle of this range (magnetic equator, dashed black line). Panels *b*, *e* exhibit the sphere-averaged HMF radial component modulus multiplied by squared distance (blue line) and the root-mean-square deviation of this value (red line). Panels *c*, *f* illustrate the relative difference between calculated and Parker HMFs, calculated from (16), averaged over longitude. Shades of blue and solid blue isolines indicate positive values; shades of yellow and red and dashed isolines, negative ones

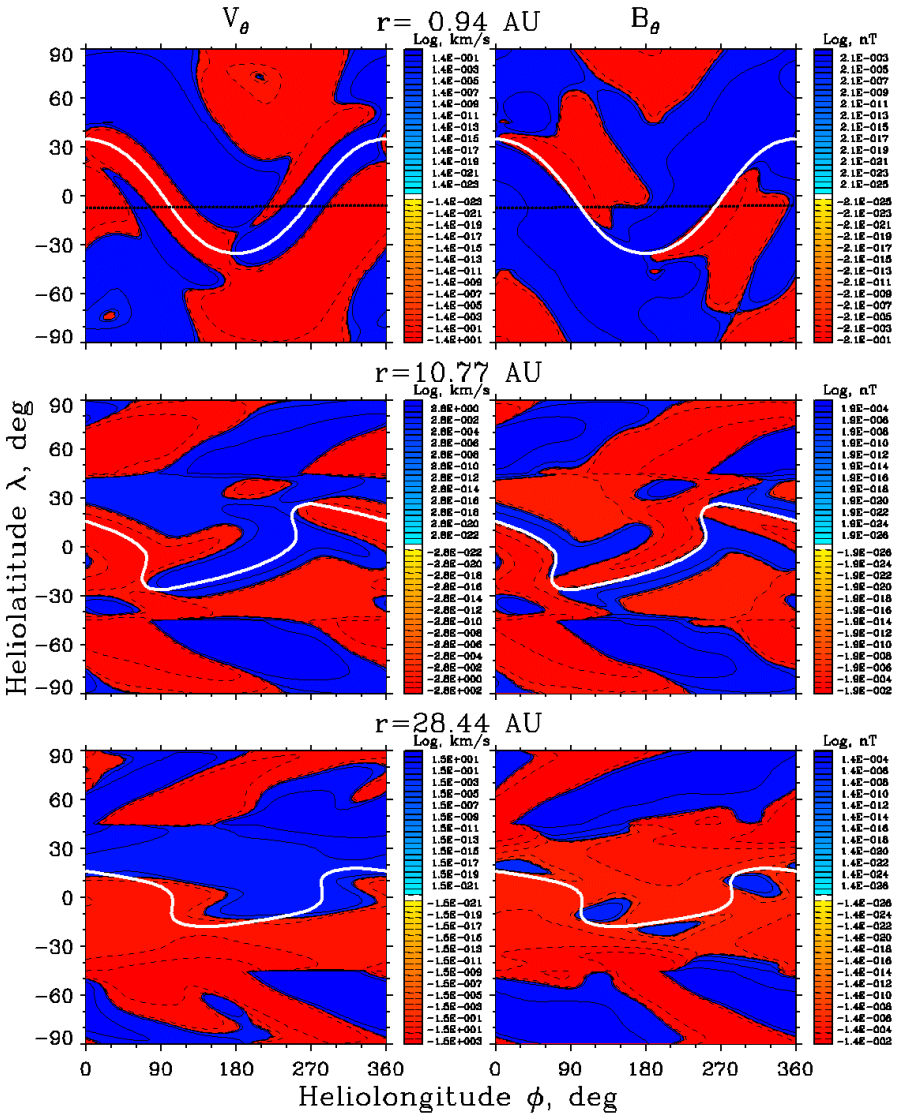

Figure 8. Distribution of polar components of SW velocity (left) and HMF induction (right) according to GONG data with L_{max}=1 at different heliocentric distances. Isoline types are the same as in Figures 3, 4. Correspondence of the color shade to the characteristic value is shown to the right of each panel. HCS lines are given by the isolines B_r=0 (white lines on the V_ϑ and B_ϑ maps)

7. For the complete model, the evolution of SW velocity and HMF distributions is largely completed by 30 AU, in contrast to the dipole model for which the slow evolution of this characteristic at 30 AU is still ongoing.

8. Coalescence of different CIRs with the formation of merged CIRs (MCIR [Richardson, 2018]) was not observed in simulations.

From the comparison between the CIR models calculated by the Russian and Chinese teams, we can draw the following conclusions:

- The HCS shape calculated in Russian models is significantly perturbed already at r=4 AU;
- The above-mentioned features of evolution with distance (the separation of CIRs from HCS, a decrease in longitude and an increase in latitude gradients of SW velocity and HMF strength, and a change in the HCS shape) are much weaker in Russian models;
- The degree of longitude uniformity of high-latitude and low-latitude meridional SW streams in the CIR models of the two teams differs significantly: The high-latitude stream (poleward) is more homogeneous in the Chinese model; whereas the low-latitude stream (equatorward) is more honogeneous in the Russian model.

In order to correct the HCS disturbance due to shortcomings of its numerical determination, it seems necessary to use an adaptive simulation mesh. As for the other two differences in the CIR models of the Russian and Chinese teams, their causes are still unclear. It seems, however, that three of the differences between the Chinese and Russian models, listed in Section 2, may play a major role in setting boundary conditions on the inner boundary of the heliosphere:

1) A different relationship between SW velocity V and density N (VN=*const* and $V^3N \approx const$) on the sphere r=0.1 AU in the Russian and Chinese models respectively;

2) The invariant T/V=*const* and T/V^2=*const* at 0.1 AU in the Russian and Chinese models respectively;

3) Significantly different values of the radial magnetic field modulus (with approximate dependence as r^{-2}) cor-

responding to B_r=4.5 nT at r=1 AU for the Russian model and $B_r \approx$ 40 nT for the Chinese model.

It is hoped that further collaborative work allows us to find the solution of these problems and to develop more reliable models of corotating interaction regions of solar wind streams of different speed.

The work of D.A. Pavlov was carried out at Leonhard Euler International Mathematical Institute in Saint Petersburg with financial support from the Ministry of Science and Higher Education of the Russian Federation (Agreement No. 075-15-2025-343 dated April 29, 2025).

We are grateful to the WSO team, as well as to the developers of the PLUTO, POT3D, and streamtracer packages.

REFERENCES

Arge C.N., Pizzo V.J. Improvement in the prediction of solar wind conditions using near-real time solar magnetic field updates. *J. Geophys. Res.: Space Phys*. 2000, vol. 105, no. A5, pp. 10465–10479. DOI: 10.1029/1999JA900262.

Arutyunyan S.N., Kodukov A.V., Subbotin M.O., Pavlov D.A. A prototype of a background solar wind forecasting service based on MHD modeling and WSA boundary conditions. *Cosmic Res*. 2023, vol. 61, no. 6, pp. 447–453. DOI: 10.1134/S0010952523700508.

Belcher J.W., Davis Jr L. Large-amplitude Alfvén waves in the interplanetary medium, 2. *J. Geophys. Res.* 1971, vol. 76, no. 16, pp. 3534–3563. DOI: 10.1029/JA076i016p03534.

Burlaga L.F., Klein L.W., Lepping R.P., Behannon K.W. Large-scale interplanetary magnetic fields: Voyager 1 and 2 observations between 1 AU and 9.5 AU. *J. Geophys. Res.: Space Phys*. 1984, vol. 89, no. A12, pp. 10659–10668. DOI: 10.1029/JA089iA12p10659.

Forsyth R.J., Gosling J.T. Corotating and transient structures in the heliosphere. *The Heliosphere Near Solar Minimum. The Ulysses Perspective*. 2001, pp. 107–166.

Gosling J.T., Pizzo V.J. Formation and evolution of corotating interaction regions and their three dimensional structure. *Space Sci. Rev*. 1999, vol. 89, no. 1, pp. 21–52. DOI: 10.1023/A:1005291711900.

Guo X., Florinski V. Corotating interaction regions and the 27 day variation of galactic cosmic rays intensity at 1 AU during the cycle 23/24 solar minimum. *J. Geophys. Res.: Space Phys*. 2014, vol. 119, no. 4, pp. 2411–2429. DOI: 10.1002/2013JA019546.

Guo X., Florinski V. Galactic cosmic-ray intensity modulation by corotating interaction region stream interfaces at 1 AU. *Astrophys. J*. 2016, vol. 826, no. 1, p. 65. DOI: 10.3847/0004637X/826/1/65.

Hoeksema J.T. Structure and Evolution of the Large Scale Solar and Heliospheric Magnetic Fields: *Thesis ... PhD in Physics, Stanford University*. 1984, 222 p.

Hundhausen A.J., Gosling J.T. Solar wind structure at large heliocentric distances: An interpretation of Pioneer 10 observations. *J. Geophys. Res*. 1976, vol. 81, no. 7, pp. 1436–1440. DOI: 10.1029/JA081i007p01436.

Kalinin M.S., Krainev M.B., Luo S., Podgiter M.S. The influence of corotating regions of interaction of the solar wind on long-term variations in the intensity of galactic cosmic rays. *Geomagnetism and Aeronomy*. 2023, vol. 63, no. 5, pp. 570–580, DOI: 10.31857/S0016794023600606.

Kalinin M.S., Krainev M.B., Luo S., Podgiter M.S. Effect of corotating interaction regions of solar wind on GCR intensity in 2D modulation problems. *Geomagnetism and Aeronomy*. 2024, vol. 64, no. 7, pp. 104–114. DOI: 10.1134/S0016793224700154R.

Krainev M.B., Kalinin M.S., Bazilevskaya G.A., Svirzhevskaya A., Svirzhevsky N., Luo Xi, Aslam O.P.M., et al. Manifestation of solar wind corotating interaction regions in GCR intensity variations *Sol.-Terr. Phys*. 2023, vol. 9, iss. 1, pp. 9–20. DOI: 10.12737/stp-91202302.

Kopp A., Wiengarten T., Fichtner H. Cosmic-ray transport in heliospheric magnetic structures. II. Modeling particle transport through corotating interaction regions. *Astrophys. J*. 2017, vol. 837, no. 1, p. 37. DOI: 10.3847/1538-4357/aa603b.

Luo X., Zhang M., Feng X., Potgieter M, Shen F., Bazilevskaya G.A. A numerical study of the effects of corotating interaction regions on cosmic-ray transport. *Astrophys. J*. 2020, vol. 899, no. 2, p. 90. DOI: 10.3847/1538-4357/aba7b5.

Luo X., Potgieter M.S., Krainev M., et al. A numerical study of the effects of a corotating interaction region on cosmic-ray transport: Some features of different cosmic-ray composition and rigidity. *38th International Cosmic Ray Conference (ICRC2023)*. Nagoya, 2023.

Luo X., Potgieter M.S., Zhang M., Shen F. A numerical study of the effects of a corotating interaction region on cosmic-ray transport. II. Features of cosmic-ray composition and rigidity. *Astrophys. J.* 2024, vol. 961, no. 1, p. 21. DOI: 10.3847/1538-4357/ad0cb6.

Mignone A., Bodo G., Massagila S., Matsakos T., Tesileanu O., Zanni C., Ferrari A. PLUTO: A numerical code for computational astrophysics. *Astrophy. J. Suppl. Ser*. 2007, vol. 170, no. 1, p. 228. DOI: 10.1086/513316.

Modzelewska R., Bazilevskaya G.A., Boezio M., Koldashov S.V., Krainev M.B., Marcelli N., Mayorov A.G., et al. Study of the 27 day variations in GCR fluxes during 2007–2008 based on PAMELA and ARINA observations. *Astrophys. J*. 2020, vol. 904, no. 3, p. 13. DOI: 10.3847/1538-4357/abbdac.

Nikolic L. Modelling the magnetic field of the solar corona with potential-field source-surface and Schatten current sheet models. *Natural Resources Canada. Geological Survey of Canada, open file*. 2017.

Parker E.N. Dynamics of the interplanetary gas and magnetic fields. *Astrophys. J*. 1958, vol. 128, p. 664. DOI: 10.1086/146579.

Pizzo V.J., Gosling J.T. 3-D simulation of high-latitude interaction regions: Comparison with Ulysses results. *Geophys. Res. Lett*. 1994, vol. 21, no. 18, pp. 2063–2066. DOI: 10.1029/94GL01581.

Potgieter M.S. Solar modulation of cosmic rays. *Living Reviews in Solar Physics*. 2013, vol. 10, pp. 1–66. DOI: 10.12942/lrsp-2013-3.

Powell K.G., Roe P.L., Linde T.J., Gombosi T.I., De Zeeuw D.L. A solution-adaptive upwind scheme for ideal magnetohydrodynamics. *Journal of Computational Physics*, 1999, vol. 154, no. 2, pp. 284–309. DOI: 10.1006/jcph.1999.6299.

Richardson I.G. Solar wind stream interaction regions throughout the heliosphere. *Living reviews in solar physics*. 2018, vol. 15, no. 1, p. 1. DOI: 10.1007/s41116-017-0011-z.

Riley P., Linker J.A., Mikic Z., Lionello R. A comparison between global solar magnetohydrodynamic and potential field source surface model results. *Astrophys. J*. 2006, vol. 653, no. 2, p. 1510.

Schatten K.H. Current sheet magnetic model for the solar corona. 1971, no. X-692-71-132.

Schatten K.H., Wilcox J.M., Ness N.F. A model of interplanetary and coronal magnetic fields. *Solar Phys*. 1969, vol. 6, pp. 442–455.

Shen F., Yang Z., Zhang J., Wei W., Feng X. Three-dimensional MHD simulation of solar wind using a new boundary treatment: Comparison with in situ data at Earth. *Astrophys. J.*

2018, vol. 866, no. 1, p. 18. DOI: 10.3847/1538-4357/aad806.
Wang Y.M., Sheeley Jr N.R. Solar wind speed and coronal flux-tube expansion. *Astrophys. J.* 1990, vol. 355, pp. 726–732.
Wang Y.X., Guo X.C., Wang C., et al. MHD modeling of the background solar wind in the inner heliosphere from 0.1 to 5.5 AU: Comparison with in situ observations. *Space Weather*. 2020, vol. 18, no. 6, p. e2019SW002262. DOI: 10.1029/2019SW002262.
Wiengarten T., Kleimann J., Fichtner H., Kühl P., Kopp A., Heber B., Kissmann R. Cosmic ray transport in heliospheric magnetic structures. I. Modeling background solar wind using the CRONOS magnetohydrodynamic code. *Astrophys. J.* 2014, vol. 788, no. 1, p. 80. DOI: 10.1088/0004-637X/788/1/80.
Zhu Y.J., Shen F., Luo X., Wang Y., Tang B. Solar energetic particles intensity variations associated with a tilted-dipole 3D corotating interaction region. *Earth and Planetary Physics*. 2024, vol. 8, no. 5, pp. 797–810. DOI: 10.26464/epp2024049.
URL: https://github.com/predsci/POT3D (accessed May 15, 2025).
URL: http://www.swpc.noaa.gov/products/wsa-enlil-solar-wind-prediction (accessed May 15, 2025).
URL: http://solarwind.entroforce.ru (accessed May 15, 2025).
URL: http://wso.stanford.edu/Harmonic.los/ghlist.html (accessed May 15, 2025).
URL: http://wso.stanford.edu/words/pfss.pdf (accessed May 15, 2025).
URL: http://wso.stanford.edu/Harmonic.los/CR2066 (accessed May 15, 2025).
URL: https://github.com/sunpy/streamtracer (accessed May 15, 2025).

The paper is based on material presented at the 20th Annual Conference on Plasma Physics in the Solar System, February 10–14, 2025, Space Research Institute RAS, Moscow, Russia.

Original Russian version: Pavlov D.A., Krainev M.B., Kalinin M.S., Kodukov A.V., Xi Luo, Fang Shen, Yuji Zhu, published in Solnechno-zemnaya fizika. 2025, vol. 11, no. 4, pp. 114–126. DOI: 10.12737/szf-114202511.

How to cite this article

Pavlov D.A., Krainev M.B., Kalinin M.S., Kodukov A.V., Xi Luo, Fang Shen, Yuji Zhu. MHD-simulation of corotating interaction regions in the heliosphere using different boundary conditions and codes. *Sol.-Terr. Phys*. 2025, vol. 11, iss. 4, pp. 104–115. DOI: 10.12737/stp-114202511.